Geophys. J. Int. (2004) **158,** 785–797 doi: 10.1111/j.1365-246X.2004.02182.x

Forms of hydrothermal and hydraulic flow in a homogeneous unconfined aquifer

László Cserepes* and László Lenkey

Department of Geophysics, Eötvös University, Pázmány Péter sétány 1/c, 1117 Budapest, Hungary. E-mail: lenl@freemail.hu

Accepted 2003 October 21. Received 2003 September 1; in original form 2002 March 22

SUMMARY

Groundwater flow in an unconfined aquifer (a porous layer with an open top) can be driven either by hydraulic forces, i.e. the gradient of the water table, or by differences in the density of porewater due to thermal expansion and changes in salinity. In this study we assume that the salinity is constant, and we investigate the spatial forms of the hydraulic and hydrothermal flows, with emphasis on the case where both components are present. Since basic flow patterns are under consideration, the simple case of a homogeneous (but anisotropic) layer is studied by numerical solution of the governing equations. When the surface hydraulic gradient is zero, free thermal convection can occur in strictly cellular forms. Just above the critical Rayleigh number the first form of convection is 2-D rolls; later square cells become stable. These flows exhibit asymmetrical patterns due to the different conditions prevailing at the top and bottom boundaries. In natural circumstances no strict cellularity can be expected: instead of regular squares, irregular polygonal cells develop and remain time-dependent. When the hydraulic governing force is added to the thermal forces, i.e. the gradient of the water table is no longer zero, first we have polygonal cells. When the hydraulic gradient increases gradually, the polygons are replaced by longitudinal rolls (i.e. rolls parallel to the gradient direction). This occurs in a regime where the hydrothermal and hydraulic governing forces are equally important. Later, when the hydraulic gradient is even higher, the flow pattern changes abruptly to transverse rolls. At low anisotropies, these transverse rolls drift with the main hydraulic flow in the direction of the slope of the water table. Finally, at strong hydraulic gradients, the cells of convection are completely suppressed by the fast hydraulic flow, which is now organized in a 'unicell' form. Domain boundaries are established for all these circulation patterns as functions of the Rayleigh number, surface hydraulic gradient and anisotropy. Characteristics of the heat transfer are also analysed.

Key words: anisotropy, convection, groundwater flow, hydrology.

INTRODUCTION

The most common driving force for groundwater flow is the horizontal pressure gradient caused by the varying height (i.e. the topography) of the water table. This type of groundwater circulation will be called hydraulic flow. Another important driving force derives from the temperature difference between the lower and upper part of the reservoir which results in variations in the density of the water due to thermal expansion. When the water flow is caused solely by the difference in density then it is called free convection. Free convection causes thermal anomalies, which may be characterized by very high horizontal temperature gradients. The topography-driven hydraulic flow also disturbs the thermal field, but its effect is less pronounced.

A frequently used tool in the study of groundwater flow is numerical modelling when the equations of hydraulics and heat transport are solved numerically. In this study we have carried out three-dimensional (3-D) model calculations to investigate the basic characteristics of hydraulically and thermally driven groundwater flow, with the main emphasis on the interaction of the two driving forces.

The flow pattern and the temperature distribution can be calculated analytically for the simplest hydraulic flow when a homogeneous horizontal layer is bounded at the top by a gentle 2-D topographic slope (Domenico & Palciauskas 1973). In more complex 2-D cases, when the hydraulic parameters of the reservoir vary, the equations can be solved numerically by finite-difference (Remson *et al.* 1971) or finite-element methods (Smith & Chapman 1983). When free convection is neglected, as in the cited examples, the theoretical problem is simple and the real significance of the models lies in their direct application to actual field studies. There are many 2-D models of such a kind, e.g. Willett & Chapman (1987), Clauser

*Deceased 2002.

& Villinger (1990), Celati *et al.* (1991), Deming (1993) and Harris *et al.* (2000). As an example of 3-D studies, the thermal effects of topography driven groundwater flow are discussed by Woodbury & Smith (1985).

The other end-member type of groundwater flow in an unconfined aquifer is free convection in the absence of a hydraulic gradient at the surface. Free convection can develop in thick layers with high permeability, e.g. in basins filled with loose sediments, and in areas having high heat flow, e.g. in active volcanic provinces. Well-known examples can be found in the ocean floor at mid-ocean ridges (e.g. Williams *et al.* 1974; Fisher *et al.* 1990; Davis *et al.* 1996). Near the spreading centres there is no sedimentary cover on the porous pillow lavas and the circulating pore water originates from and enters back into the sea, thus representing convection in an unconfined porous reservoir. 2-D modelling of free convection in the ocean floor was carried out by Ribando *et al.* (1976) and Rosenberg & Spera (1990) for example. Certain 3-D models of free convection in the ocean floor (Williams *et al.* 1986; Rabinowicz *et al.* 1998) can be adopted for unconfined aquifers in sediments. Bus & Cserepes (1994) investigated 3-D free convection in rectangular cells and found a structure which is stable over a wide range of Rayleigh numbers. It consists of asymmetric currents with wide downwellings in the centre of the cells and narrow upwellings along the cell peripheries.

A third form of flow is free convection in a confined aquifer, i.e. in a horizontal layer with impermeable boundaries. This has been the basic model in many studies of porous convection. The layer is assumed to be homogeneous and isotropic, having no externally imposed hydraulic gradient (as is natural in free convection). In the linear approximation of the theory Beck (1972) has shown that convection in a layer with an isothermal top and bottom begins in the form of 2-D rolls when the Rayleigh number R exceeds $R_{\rm crit} = 4\pi^2 = 39.5$, and the 3-D modes exist when $R > 4.5\pi^2 = 44.4$. Carrying out an eigenfunction-expansion stability analysis, Steen (1983) has proved that the so-called [111] cubic cell mode becomes stable for $R > 4.87\pi^2 = 48.06$. This mode is symmetric; the spatial forms of the downgoing and upgoing currents are identical. Schubert & Straus (1979) found that the steady cubic-cell flow is replaced by a time-dependent oscillatory regime at high Rayleigh numbers. Improving the numerical accuracy of the computations, Kimura *et al.* (1989), Stamps *et al.* (1990) and Graham & Steen (1991) located the transition of the [111] mode from the steady to the oscillatory state at $R = 580$.

As a fourth class of flow, a special type of free convection occurs in a dipping confined permeable layer. If the lower and upper impermeable boundaries are isothermal and the lower is warmer, then free convection develops even in the case of very small subcritical Rayleigh numbers, because the buoyancy force has a component parallel to the layer. This so-called basic flow has one cell, which occupies the whole layer. When the Rayleigh number exceeds the critical value depending on the dip of the layer, multicell convection begins (Bories & Combarnous 1973; Caltagirone & Bories 1985; Bernard 1988; Ormond & Genthon 1993; Wang *et al.* 1997). In the case of small dips polygonal cells are obtained, while for larger dips quasi 2-D longitudinal rolls develop, their axis being parallel to the slope. These flow patterns can be regarded as a superposition of the basic flow and the cellular free convection.

In this study we deal with a combination of the first and second type of groundwater flow, i.e. with the interaction of the topography-driven hydraulic flow and free convection in a reservoir, which is unconfined at the surface. As we shall see, this mixed kind of circulation has a close relationship with the third and fourth type of water flows mentioned above. We assume a layer bounded by an impermeable bottom and a permeable top. The boundaries are isothermal. The condition for the onset of free convection is fulfilled. Additionally, a non-zero hydraulic gradient is prescribed at the surface. The main goal is to study the resulting 3-D circulation patterns. We shall use numerical methods to model the groundwater flow.

The selected model can be applied to real situations. The topography-driven hydraulic flow is the most common type of flow in unconfined reservoirs and sometimes the condition for free convection is also fulfilled. The variation of the topography in the Great Hungarian Plain drives the groundwater flow in the upper 1 km of the sediments (Erdélyi 1985). In the Tiszakécske area, located in the plain, the permeability of the sediments is higher than the average and the thickness of the permeable sediments is large enough for the onset of free convection (Alföldi *et al.* 1976; Lenkey 1993). Thus, in this area both types of groundwater flow occur simultaneously. Modelling the Campiglia hydrothermal system (Tuscany, Italy), Celati *et al.* (1990) conclude that the same situation is found here. In the Campiglia hydrothermal system the high background heat flux of the area also contributes to the development of free convection.

Our aim here is not the construction of flow models for particular areas. What we want to show here is the fundamentals of the combined hydraulic–thermal flow. In the first part of the paper we summarize the forms of free convection in an unconfined layer (without hydraulic flow), which help to better understand the forms of the combined flow. We investigate the effects of anisotropy on the critical Rayleigh number, wavelength of convection cells and heat transport. The main part of the paper is devoted to showing the different forms of the combined hydraulic–thermal flow, which have not been investigated before. We also establish the conditions for their formation. In the next section we define the model and describe the mathematical method employed.

DESCRIPTION OF THE MODEL

The model consists of a rectangular box of a horizontal homogeneous permeable layer (Fig. 1). The lower boundary is impermeable, the upper boundary is open, which is equivalent to the assumption that it is a free water table. The upper boundary has a constant slope, γ, in the x direction. The $x = 0$ and $x = D_x$ sides of the box are assumed to be symmetry planes. This implies that there is no flow across these boundaries. Similarly, mirror symmetry is imposed on the $y = 0$ and $y = D_y$ surfaces. Due to the mirror symmetry on the sides of the box the flow in the layer is horizontally periodic with

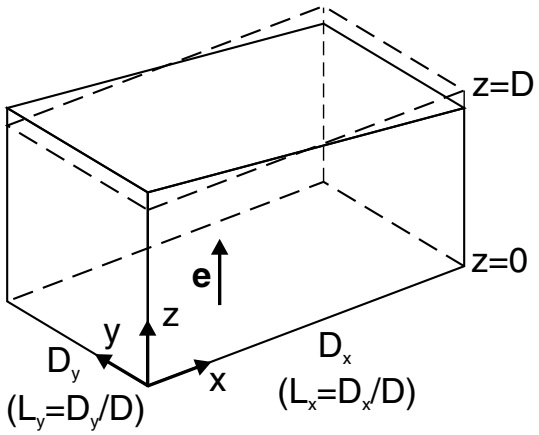

Figure 1. Coordinate system of the computational domain.

periods D_x and D_y in the x and y directions respectively. If there were no other driving force than the hydraulic gradient arising from the slope of the surface, a 2-D hydraulic flow would develop in the (x, z) plane. The boundary condition for the temperature is $T = 0$ on the surface and $T = \Delta T > 0$ on the bottom. If ΔT is large enough, 3-D thermal convection is obtained.

The two general equations governing the flow in a permeable medium are the equation of continuity and Darcy's law (Marsily 1986; Bear & Verruijt 1987):

$$\frac{\partial(n\rho)}{\partial t} + \nabla(\rho \mathbf{u}) = 0 \tag{1}$$

$$-\rho g \mathbf{e} - \nabla p - \eta \boldsymbol{k}^{-1} \mathbf{u} = 0 \tag{2}$$

where ρ is the density of water, n is the porosity of the layer, $\mathbf{u}$ is the Darcy velocity (filtration flux), g is the gravitational acceleration, $\mathbf{e}$ is the vertical unit vector pointing upward, p is the pressure, η is the viscosity of the water and $\boldsymbol{k}$ is the permeability tensor. In a multilayered sedimentary sequence, where silty, clayey layers are interbedded between sandstone layers the average horizontal permeability is generally much larger than the average vertical permeability. We chose a diagonal permeability tensor composed of k_0 permeability in x and y directions and k_0/ε permeability in the z direction. $\varepsilon > 1$ is the anisotropy coefficient. It is defined as the ratio of horizontal to vertical permeabilities.

Assuming thermal equilibrium between the water and the medium the temperature distribution is governed by the heat transport equation (e.g. Marsily 1986):

$$\chi \frac{\partial T}{\partial t} + \mathbf{u} \nabla T = \kappa \nabla^2 T \tag{3}$$

where $\chi = \rho_m c_m / \rho_0 c_0$ and $\kappa = \lambda_m / \rho_0 c_0$. ρ_m, c_m and λ_m are the density, specific heat and heat conductivity of the water-saturated medium and ρ_0, c_0 are the density (at $T = 0$) and specific heat of the water. For simplicity we assume that $\chi = 1$.

Applying the Boussinesq approximation, introducing the poloidal potential, V, and using dimensionless variables the governing eqs (1)–(3) become:

$$\varepsilon \left(\frac{\partial^2 V}{\partial x^2} + \frac{\partial^2 V}{\partial y^2} \right) + \frac{\partial^2 V}{\partial z^2} = RT \tag{4}$$

$$\frac{\partial T}{\partial t} + \mathbf{u} \nabla T = \nabla^2 T \tag{5}$$

where R is the Rayleigh number

$$R = \frac{k_0 \alpha \rho_0 g \Delta T D}{\eta \kappa} \tag{6}$$

and α is the thermal expansion coefficient of water. The filtration flux, $\mathbf{u} = (u, v, w)$ can be derived from V as:

$$u = \frac{\partial^2 V}{\partial x \partial z}, \quad v = \frac{\partial^2 V}{\partial y \partial z}, \quad w = -\left(\frac{\partial^2 V}{\partial x^2} + \frac{\partial^2 V}{\partial y^2} \right). \tag{7}$$

Eqs (4)–(7) are derived in the Appendix. The dimensionless width of the box is $L_x = D_x/D$ in the x direction and $L_y = D_y/D$ in the y direction. The boundary conditions at the top of the model box become:

$$T = 0, \qquad \frac{\partial V}{\partial z} = G\left(x - \frac{L_x}{2} \right) \quad \text{at} \quad z = 1 \tag{8}$$

where G is the dimensionless dip of the slope

$$G = \frac{k_0 \rho_0 g D}{\eta \kappa} \gamma. \tag{9}$$

On the bottom and the sides of the box the boundary conditions are the following:

$$T = 1 \quad \text{and} \quad V = 0 \quad \text{at} \quad z = 0 \tag{10}$$

$$\frac{\partial T}{\partial x} = 0 \quad \text{and} \quad \frac{\partial V}{\partial x} = 0 \quad \text{at} \quad z = 0, L_x \tag{11}$$

$$\frac{\partial T}{\partial y} = 0 \quad \text{and} \quad \frac{\partial V}{\partial y} = 0 \quad \text{at} \quad y = 0, L_y. \tag{12}$$

The problem is defined by the eqs (4)–(12). The free (input) parameters are ε , R, G, L_x, L_y and the initial conditions in eq. (5).

The system of eqs (4)–(7) is solved on an equally spaced grid by finite differences. In eq. (5) the advective terms are calculated by central spatial differences. Eq. (5) is solved by the alternating direction implicit iteration. Eq. (4) is Fourier transformed in the horizontal directions and then solved in the spectral space. In the vertical direction it is solved by finite differences. The iteration in time is carried out until a steady or quasi-steady state is reached. The numerical method is the same as described in Cserepes *et al.* (1988) and Bus & Cserepes (1994).

CONVECTION IN THE CASE OF A HORIZONTAL WATER TABLE ($G = 0$)

A starting case for our models is when the hydraulic gradient on the surface is zero ($G = 0$): then the water table is horizontal. In this case there is no groundwater motion except if the Rayleigh number is higher than the critical value (R_{cr}). This is free convection.

When R is only slightly higher than R_{cr}, a stable 2-D convection pattern exists in the form of 2-D rolls. The same has been found for hydrothermal convection in a homogeneous layer below an impermeable boundary (Steen 1983) and for the convection of a Newtonian fluid (Busse & Whitehead 1971; Bolton & Busse 1985).

Table 1 shows the critical Rayleigh numbers for a permeable upper boundary and three cases of the anisotropy coefficient ($\varepsilon = 1$, 10, 100) and, as a comparison case, for an impermeable upper boundary and $\varepsilon = 1$. The table also contains the wavenumbers a_{cr} for the onset of convection at the critical Rayleigh number. In the next row the width of the rolls ($L/2$) for $R = R_{cr}$ can be seen. L is the wavelength of the convection, i.e. the width of two neighbouring rolls turning in opposite sense ($L = 2\pi/a$). The larger the anisotropy coefficient, the larger L is, because $\varepsilon > 1$ means that the hydraulic conductivity is larger horizontally than vertically. The increase of the characteristic horizontal length with the increase of ε will be shown in examples later.

As the Rayleigh number increases, the width of the rolls decreases. Fig. 2 shows the half-wavelengths ($L/2$) for $\varepsilon = 1$, 10, 100 as a function of the Rayleigh number. These are the half-wavelengths

Table 1. Upper part: critical Rayleigh numbers (R_{cr}), wavenumbers (a_{cr}) and roll widths ($(L/2)_{cr}$) for the onset of free convection. Lower part: critical Rayleigh numbers ($R_{cr,3D}$) for the stability of square cells with selected width (L). ε is the anisotropy coefficient.

	Permeable top			Impermeable top
	$\varepsilon = 1$	$\varepsilon = 10$	$\varepsilon = 100$	$\varepsilon = 1$
R_{cr}	27.1	153	1169	$4\pi^2 = 39.5$
a_{cr}	2.300	1.425	0.895	π
$(L/2)_{cr}$	1.366	2.205	3.510	1
$R_{cr,3D}$	53.6	226	1630	48.1
	at $L = 2.4$	at $L = 4.0$	at $L = 6.4$	at $L = \sqrt{2}$

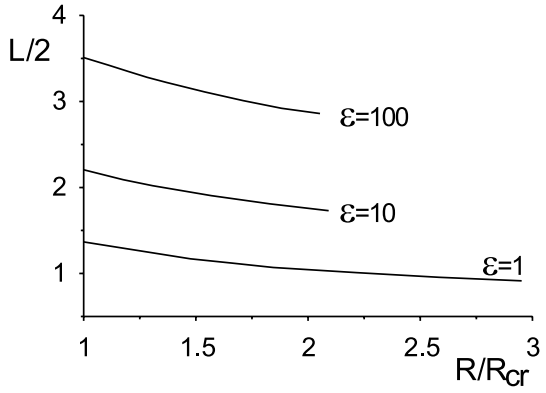

Figure 2. Width ($L/2$) of the 2-D rolls as a function of the Rayleigh number R, for various anisotropies.

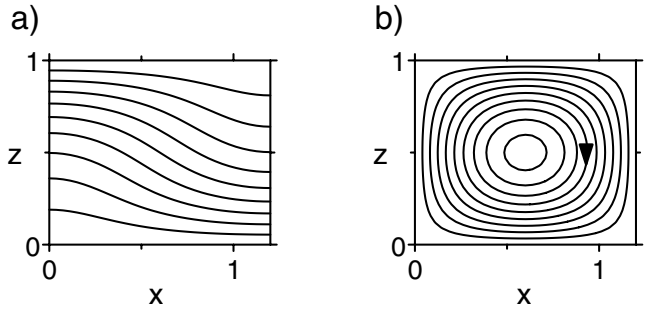

Figure 4. Vertical section of a 2-D convective roll beneath an impermeable surface for $\varepsilon = 1$, $R = 45$, $L/2 = 1.2$: (a) isotherms with a contour interval of 0.1, (b) streamlines.

at which the growth rate of a 2-D cosine-type temperature disturbance, superimposed on the conductive steady temperature field, is the largest. If the initial temperature disturbance is:

$$\delta T(x, y, z, t = 0) = A \cos \frac{2\pi x}{L} \sin \pi z \quad (A \ll 1) \tag{13}$$

its increase begins as

$$\delta T = A \cos \frac{2\pi x}{L} \sin \pi z e^{\sigma t} \tag{14}$$

where σ is the growth rate.

In the following numerical examples which have been calculated for low supercritical Rayleigh numbers, the half-wavelengths will be fixed as 1.2, 2.0 and 3.2 for $\varepsilon = 1$, 10 and 100 respectively, based on the results of Fig. 2.

Fig. 3 shows the structure of 2-D rolls at selected Rayleigh numbers in the case of an unconfined reservoir with a horizontal water table. For comparison, the flow pattern in the case of an impermeable upper boundary can be seen in Fig. 4. Similar results were presented by Ribando *et al.* (1976) for an isotropic layer. Comparison of the results for the two kinds of boundary conditions at the top reveals an important difference: beneath an impermeable boundary the cells are symmetric, while in the case of the permeable top (Figs 3a–c) they are asymmetric. Asymmetry means that the upwelling flow is narrower and more intense than the downwelling one, which is wider. The roll occurring beneath an impermeable top (Fig. 4) shows central symmetry: the up- and downwellings are mirror images of each other.

Increasing the Rayleigh number, an interval is found not too high above the critical value, where 3-D convection in square cells is stable. This form can be reached by adding the following disturbance to the conductive steady-state temperature field:

$$\delta T = A \left(\cos \frac{2\pi x}{L} + \cos \frac{2\pi y}{L} \right) \sin \pi z. \tag{15}$$

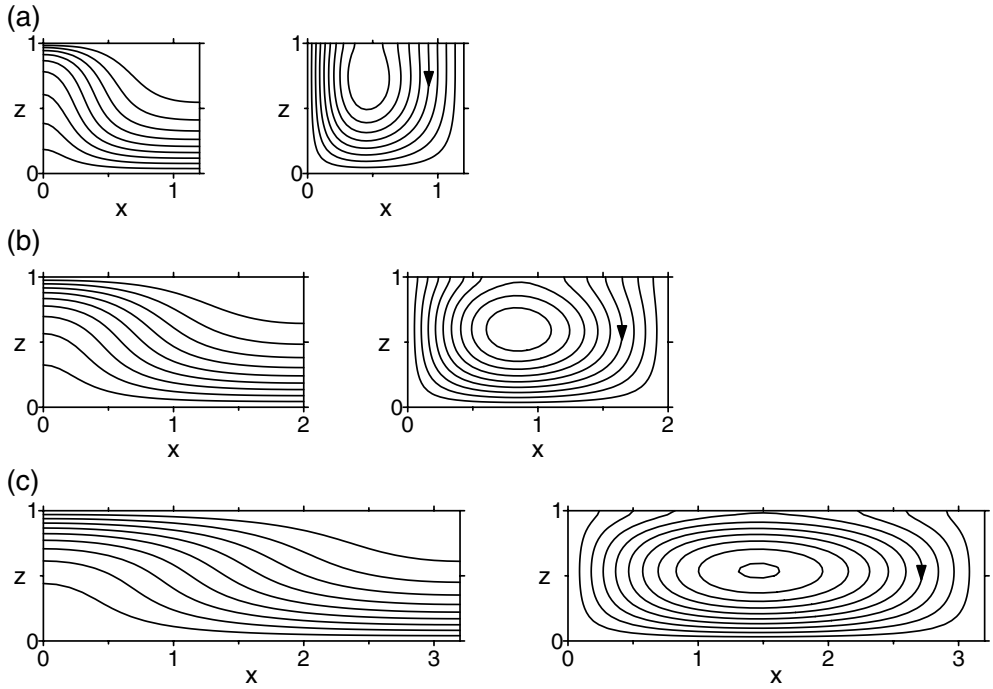

Figure 3. Vertical section of 2-D convective rolls beneath a permeable surface: (a) $\varepsilon = 1$, $R = 45$, $L/2 = 1.2$; (b) $\varepsilon = 10$, $R = 200$, $L/2 = 2.0$; (c) $\varepsilon = 100$, $R = 1500$, $L/2 = 3.2$. Isotherms with a contour interval of 0.1 are drawn in the left-hand figures, and streamlines in the right-hand figures.

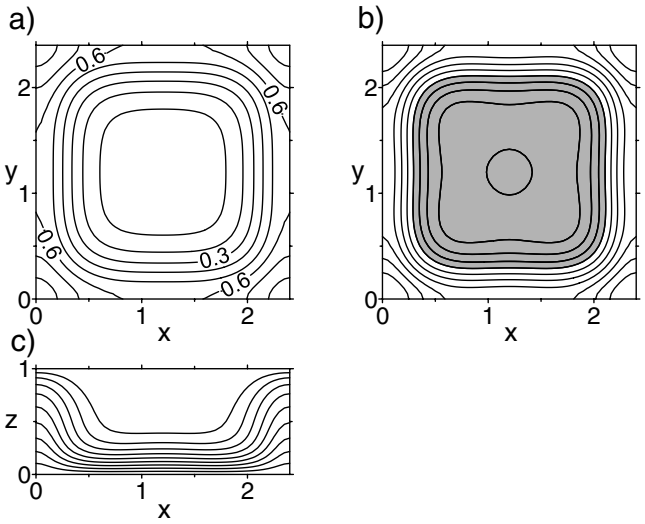

Figure 5. Structure of a square cell beneath a permeable surface $R = 60$, $L = 2.4$: (a) isotherms in the horizontal mid-plane $z = 0.5$; (b) contours of the vertical velocity in the plane $z = 0.5$. The area of the downwelling is shaded. (c) Isotherms drawn with a contour interval of 0.1 in the vertical plane $y = 1.2$.

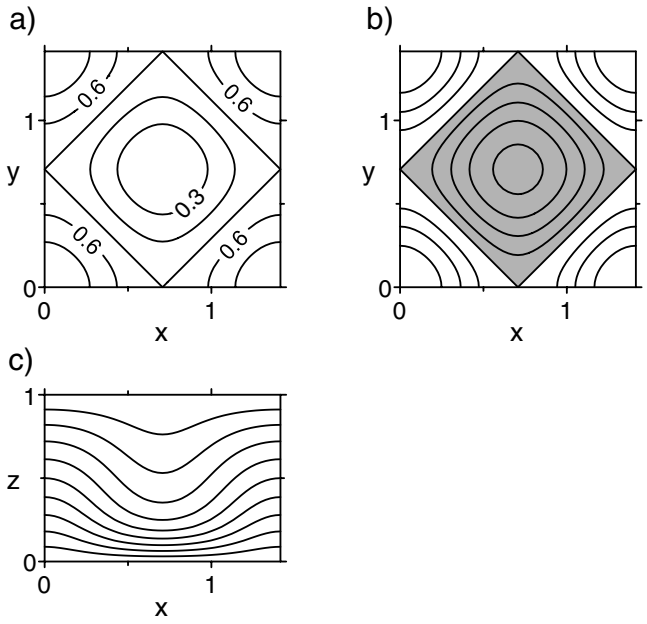

Figure 6. Structure of a square cell beneath an impermeable surface for $\varepsilon = 1$, $R = 60$, $L = \sqrt{2}$: (a) isotherms and (b) contours of the vertical velocity in the mid-plane $z = 0.5$. (c) Isotherms in the vertical plane $y = \sqrt{2}/2$. Contours and shading as in Fig. 5.

The disturbance can be regarded as the superposition of two rolls perpendicular to each other. The disturbances in eq. (15) generate square cells with a side length of $L_x = L_y = L$. The structure of the square cells is shown in Fig. 5 for $\varepsilon = 1$. The width of the box equals the wavelength L selected above from Fig. 2. The Rayleigh number is now higher than in Fig. 3(a) and the structure is stable at this R. Fig. 5 does not show solutions for high anisotropies because the pattern would be very similar to the presented structure, the only exception being that the cells are larger for $\varepsilon = 10$ or 100. The most remarkable feature of the cells is that they are asymmetric: upwelling is found all along the sides and a wide downwelling occupies the centre, i.e. the spatial forms of the up- and downwellings are different.

The comparison case for an impermeable top and bottom can be seen in Fig. 6, for $\varepsilon = 1$. The convection cell is symmetrical: the up- and downwellings occupy the same area in the mid-plane of the cell, and they are mirror images of each other (chequerboard pattern). This symmetry has already been mentioned in the introduction as a basic property of the [111] mode convection. The cell shown in Fig. 6 is the same as the [111] type convection cell discussed by Holst & Aziz (1972), Straus & Schubert (1979) and Steen (1983), except that their coordinate system is rotated by 45° compared with ours.

Square cells can be established only above a certain Rayleigh number. Below this value 2-D rolls develop even from the square-type initial conditions of eq. (15). The square cell is unstable at low Rayleigh numbers: round-off errors of the computation are enough to destroy and transform it into rolls. The stability limit of the square cells (critical Rayleigh number $R_{\mathrm{cr,3D}}$) as a function of cell size L and for $\varepsilon = 1$, 10, 100 has been established by numerical experiments (Fig. 7). The critical value strongly depends on L. The larger L is, the smaller the Rayleigh numbers which allow stable square cells. Naturally, above very large values of L the square cells become unstable again and they are transformed into rolls or smaller square cells.

It is interesting to compare the heat transport of the square cells and rolls. The non-dimensional heat transport is given by the Nusselt number:

$$Nu = \left\langle -\frac{\partial T}{\partial z} \right\rangle \tag{16}$$

where $\langle\rangle$ means averaging on the upper boundary of the cell.

The [111] type convection cell with impermeable upper and lower boundaries transports less heat below $R = 97$ than the 2-D roll convection (Straus & Schubert 1979). However, according to Steen (1983), the [111] mode is already stable from $R = 48.1$ (see Table 1). A similar phenomenon for convection in unconfined reservoirs can also be observed, but only with large anisotropy. Dashed lines in Fig. 7 show the limits of the Rayleigh number below which the rolls produce larger Nusselt numbers than square-cell convection. In this region of R square-cell convection can be stable, but transports less heat than roll convection. The extent of this region depends on the anisotropy: it is the widest for $\varepsilon = 100$ and narrower for $\varepsilon = 10$. In the isotropic case ($\varepsilon = 1$), when the square cells are stable they transfer more heat than roll convection.

We have also carried out numerical experiments in large boxes with random ('white noise') initial conditions. This is probably closer to natural conditions than the regular starting perturbations of eq. (15). The random initial conditions result in irregular cells, which do not usually reach a steady-state but oscillate irregularly. A snapshot of such a convection can be seen in Fig. 8. The model was calculated for an isotropic medium with a box size of $L_x = L_y = 7.2$ and $R = 140$. As the results of stability study for the square-cell convection show (Fig. 7), 3-D convection is expected at this Rayleigh number. The isotherms depict irregular polygonal cells with a wide cold spot, i.e. a downwelling recharge zone in their centre, and narrow upwellings (discharge zones) at the cell boundaries. Thus, the same asymmetry exists here as in the case of square cells. The structure is changing continuously. Large cells split to smaller ones and other cells merge. Note that the final state will also be irregular and

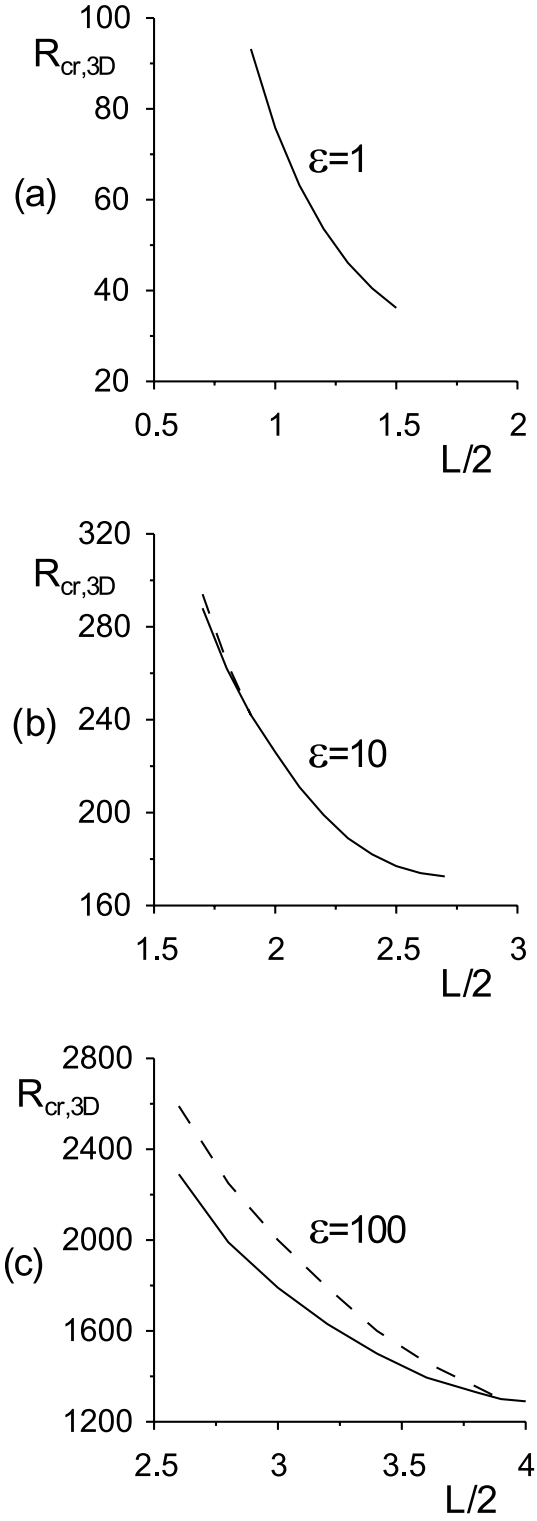

Figure 7. Stability boundary (solid lines) for the square cells as a function of the size of the squares for three different anisotropies. ($L/2$ is the half of the side of the squares.) Below the solid lines 2-D rolls are the stable solution. Below the dashed lines in (b) and (c), the rolls produce higher heat flux than the squares.

time-dependent if regular square cells which are too small or too large are forced into a large box initially. Then the instability of the cells will lead to their reshaping and a time-dependent convection develops.

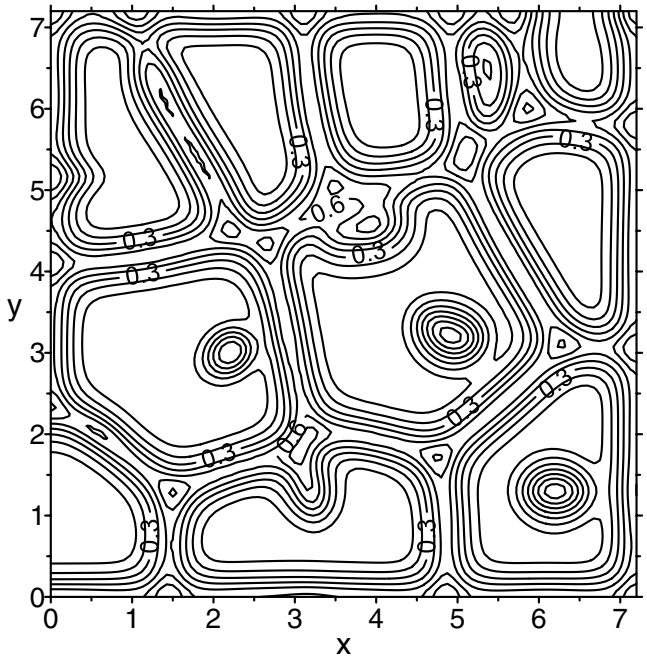

Figure 8. Irregular polygonal cells of free convection beneath a permeable surface: $\varepsilon = 1$, $R = 140$. Isotherms in the horizontal mid-plane $z = 0.5$, drawn with a contour interval of 0.1. The cell interiors are cold.

CONVECTION BENEATH A DIPPING WATER TABLE ($G > 0$)

If the water table dips ($G > 0$), there is always groundwater flow, independently of the value of the Rayleigh number R. If $G > 0$ and $R > R_{cr}$, then the two parameters, more exactly the interaction of the two driving forces characterized by the two parameters, determine the structure of groundwater flow. It is seen from eqs (6) and (9) that the governing factor is the ratio of the dip to heat expansion ($G/R = \gamma/\alpha\Delta T$). The results of modelling will be presented as the function of G and R. Many numerical experiments were carried out for the anisotropy coefficients 1, 10 and 100. The width of the model boxes was much larger than their thickness. This geometry reflects that in natural circumstances the length of a hydraulic slope, the distance from water divide to water divide, is usually much larger than the depth of the reservoir. The domains of the different flow structures found in the (G, R) space are shown in Fig. 9. The calculations were made in rectangular boxes with widths of $L_x = L_y = 7.2$, $L_x = L_y = 10$ and $L_x = L_y = 15$ for $\varepsilon = 1$, 10 and 100 respectively. The initial conditions were no flow in the box and a random temperature perturbation superimposed on the conductive equilibrium temperature field.

Three regions of the (G, R) plane can be distinguished where the structure of the flow is significantly different (Fig. 9). As the characteristics of the flow depend essentially on the G/R ratio, the boundaries of the regions for larger R shift towards larger G. For R values where 3-D convection occurs already at $G = 0$, the three regions in the order of increasing G are the following: (1) time-dependent 3-D cells (polygons), (2) longitudinal rolls, (3) 2-D flow in the direction of the slope.

Time-dependent polygonal cells

Time-dependent polygonal flow develops when R is high enough for stable 3-D convection, but G is low. The structure of the cells

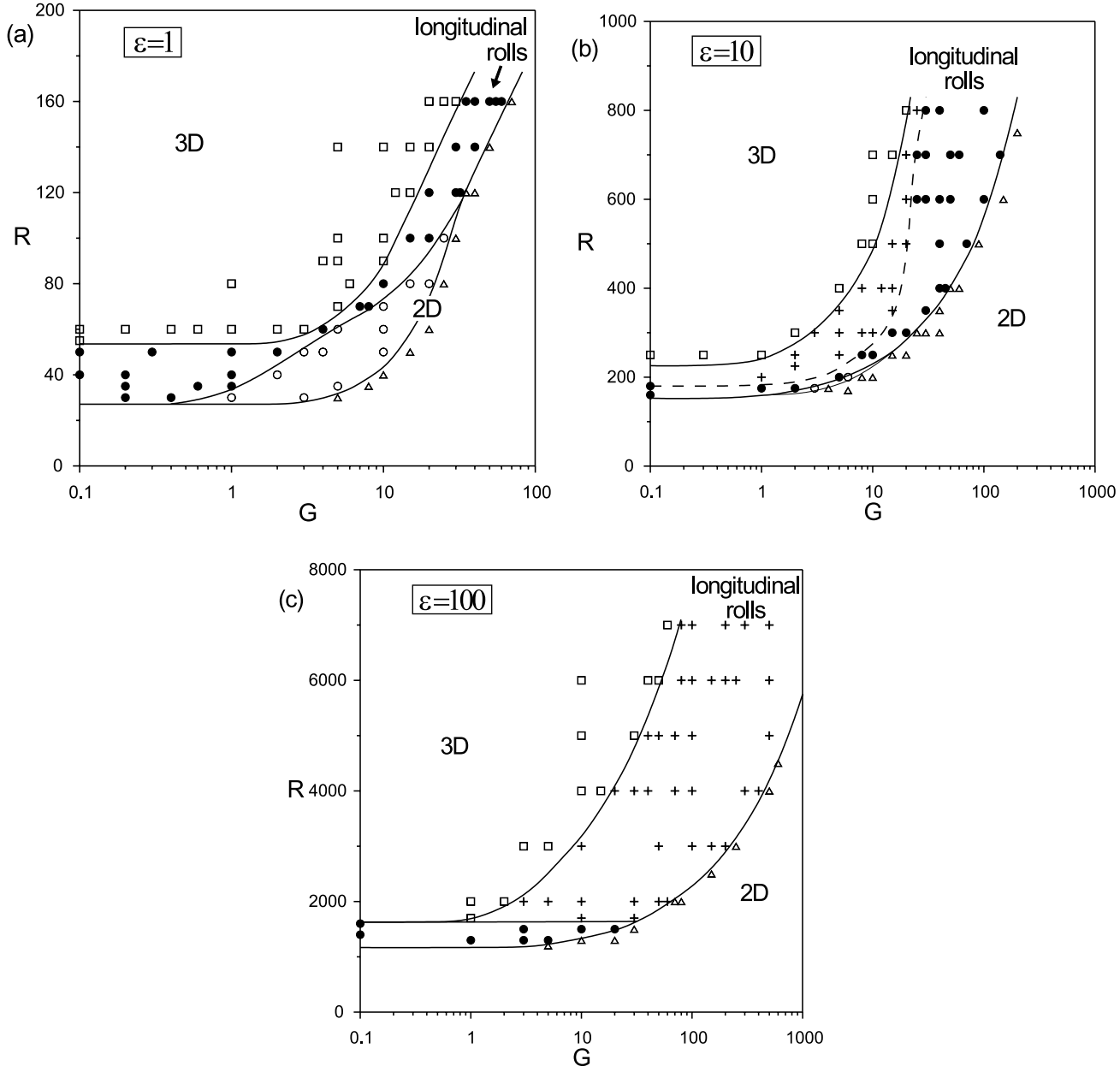

Figure 9. Domain diagrams (G, R) for the different flow patterns: (a) numerical experiments made in a box with $L_x = L_y = 7.2$, for $\varepsilon = 1$; (b) $L_x = L_y = 10$, $\varepsilon = 10$; (c) $L_x = L_y = 15$, $\varepsilon = 100$. Symbols: squares, time-dependent polygonal cells; crosses, irregular time-dependent longitudinal rolls; solid circles, regular steady-state longitudinal rolls; open circles, drifting transverse rolls; triangles, steady-state 2-D unicell flow.

is very similar to that found without a hydraulic slope (Fig. 8). The difference is that in case of a finite dip there is a net mass flux in the direction of the slope. The dip component of the velocity can be calculated by averaging the velocities for many cells. This net flux causes the cells to migrate slowly in the slope direction. If G is large enough, new cells are born at the summit of the slope, and by more or less keeping their shape they move toward the topographic low. They disappear at the lower end of the slope. In summary, in this region, where G/R is small, the structure of the flow is determined by the forms of cellular free convection. The effect of the hydraulic slope is secondary, and the interaction of the convection and hydraulic flow is weak.

Longitudinal rolls

Longitudinal rolls develop at medium G/R values. In this region the hydraulic gradient and thermal buoyancy have more or less equal importance in determining the structure of the flow. The longitudinal rolls are shown in Fig. 10 for the three anisotropy values $\varepsilon = 1$, 10, 100.

Typically in the isotropic case ($\varepsilon = 1$), steady-state solutions are obtained, at least in the investigated range of R (below $R = 160$). The structure of the flow consists of identical rolls ('cells'). The width of the rolls quickly reduces with the increase of R and G. For instance, three longitudinal cells (six rolls) develop at $R = 40$ in a

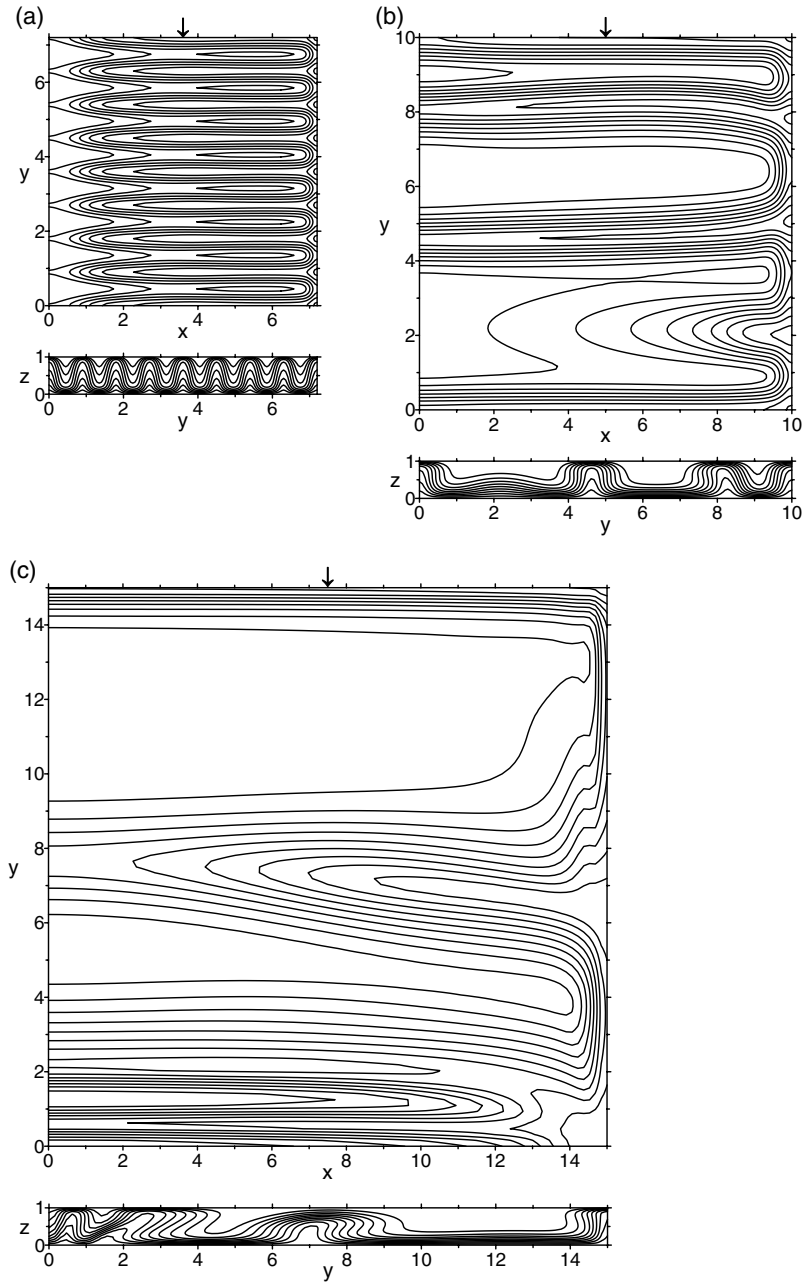

Figure 10. Examples of the longitudinal rolls. Isotherms are drawn in each panel with a contour interval of 0.1. (a) Steady-state solution for $\varepsilon = 1$, $R = 120$, $G = 20$, $L_x = L_y = 7.2$. Upper panel: horizontal section in the mid-plane $z = 0.5$. Lower panel: vertical section at $x = 3.6$. (b) A snapshot of a time-dependent solution for $\varepsilon = 10$, $R = 400$, $G = 15$, $L_x = L_y = 10$. Upper panel: horizontal section at $z = 0.5$; lower panel: vertical section at $x = 5$. (c) A snapshot for $\varepsilon = 100$, $R = 5000$, $G = 100$, $L_x = L_y = 15$. Upper panel: horizontal section at $z = 0.5$; lower panel: vertical section at $x = 7.5$. At the sides of each horizontal section arrows show the position of the corresponding vertical sections. In the horizontal section (upper panels) the water table dips to the right.

box with $L_x = L_y = 7.2$. The cell width, equal to the wavelength is $7.2/3 = 2.4$. At $R = 120$, eight or nine cells, and at $R = 160$, ten or eleven cells are obtained in the same box, depending on G. At a fixed R, the increase of G also increases the number of the cells, e.g. at $R = 120$, eight and nine cells are found for $G = 20$ and 30, respectively. In the example of Fig. 10(a), eight cells (16 counter-rotating rolls) can be seen at $R = 120$ and $G = 20$. The tendency of the decrease of the cell width with the increase of R is similar to the results found for free convection (Fig. 2), but now the decrease is faster which suggests the strong effect of the hydraulic gradient imposed on the upper boundary.

The thermal structure of the longitudinal rolls can be seen in Fig. 10(a) which shows the mid-plane of the box and a transverse vertical section across the rolls. The flow has two components: a regional flow in the direction of the slope and a convective flow which is basically perpendicular to the former one. The net flow derives from the superposition of these flow components and therefore water filtration occurs along spiral paths.

In the studied anisotropic cases ($\varepsilon = 10$, 100) the longitudinal rolls are mostly irregular and time-dependent. For $\varepsilon = 10$, time-dependent structures can be found in a large part of the domain of the longitudinal flow in the (G, R) plane (where G is smaller).

When G is larger, the structures are steady and similar to the one in Fig. 10(a). The time-dependent state means that the number, shape and size of the rolls varies, new rolls are born and others disappear. A snapshot of a time-dependent structure is shown in Fig. 10(b). Time-dependence is more enhanced for $\varepsilon = 100$. Steady-state longitudinal rolls exist only in a narrow stripe of the (G, R) plane, for small R values (Fig. 9c). Fig. 10(c) presents a snapshot of a time-dependent solution with rolls of different width. The two large rolls are just squeezing out the small ones (towards the left end of the box in the vertical cross-section). The panels of Fig. 10 prove again that the increase in anisotropy results in an increase in cell width.

The stability domain of the longitudinal rolls in the (G, R) plane is shown in Fig. 9 for the three cases of anisotropy studied. At high R values, the domain boundaries are close to the lines of $G/R=$ constant, although they are not parallel to them: for increasing values of R, the domain shifts towards larger values of G. For small, but still supercritical values of R, the roll domain turns to 'horizontal'. In the limit $G = 0$, the roll domain approaches the interval in which the 2-D rolls of free convection are stable.

The domain boundaries have been obtained by interpolation using the results of numerical experiments made in different points of the (G, R) plane. Towards the region of the time-dependent polygonal cells (towards higher R values if G is fixed) it is difficult to establish a sharp boundary, because just across the boundary the polygons are elongated in the direction of the slope and behave as quasi-rolls. There is in fact a narrow transitional zone between the domains of the polygonal cells and the longitudinal rolls. The other boundary of the roll domain (towards small values of R) is sharp, because the structure of the flow is completely different beneath this boundary.

Two-dimensional flow

Two-dimensional circulation is obtained when the value of G/R is large. In this case the dominating driving force of the flow is the hydraulic slope. The flows are 2-D in the sense that in the transverse direction (perpendicularly to the slope) all quantities are constant. A special case is the purely hydraulic flow, when $R = 0$ and G is non-zero.

There are two different types of 2-D flow. For moderate values of G/R, time-dependent transverse rolls develop which drift in the direction of the slope. This circulation mode has been found to exist for $\varepsilon = 1$ and 10, but not for $\varepsilon = 100$. It is more characteristic of the isotropic case ($\varepsilon = 1$). If exists, it is restricted to a closed zone of the (G, R) plane below a certain value of R (Fig. 9). This zone is very narrow at $\varepsilon = 10$.

The structure of the transverse rolls in a vertical section is shown in Fig. 11. The parameters of the model example are the following: isotropic medium ($\varepsilon = 1$), 7.2 for the box width, $R = 60$ and $G = 6$. Figs 11(a) and (b) depict a snapshot of the temperature distribution and the streamlines respectively. The main recharge area (top of the slope) is at the left end of the box: here the flow is directed downwards constantly. The transverse rolls are born at some distance from the left side of the box. There are four upwellings in the figure at the moment of the snapshot. The rightmost one is permanent (this is the main discharge zone at the deepest point of the surface slope), the other three move rightwards with a velocity which would be approximately the velocity of the purely hydraulic flow ($R = 0$). When the closest one reaches the end of the box, it merges into the fourth upwelling. The process is repeated regularly. During these periods the mean surface heat flux oscillates according to Fig. 11(c). The period is complicated: there are three heat flux maxima with

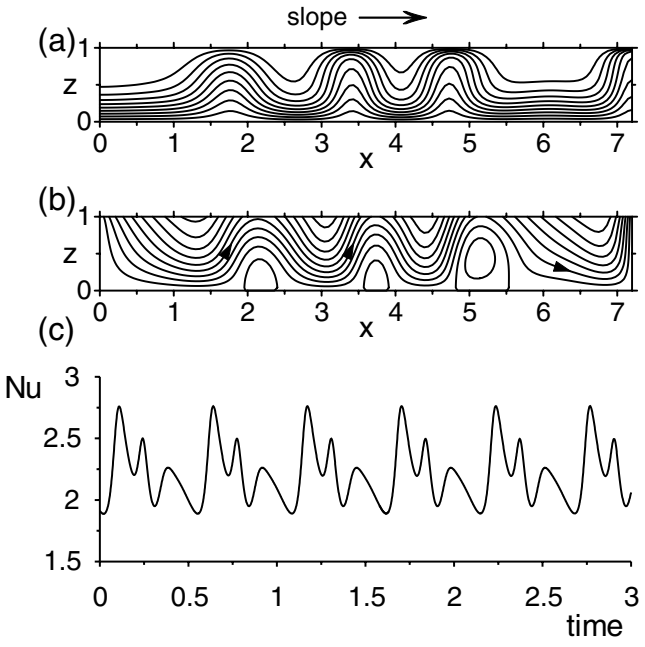

Figure 11. Snapshot of the drifting transverse rolls for $\varepsilon = 1$, $R = 60$, $G = 6$ in a box of length $L_x = 7.2$: (a) vertical section of the isotherms, contoured at intervals of 0.1; (b) vertical section of the streamlines; (c) temporal variation of the heat flux Nu.

different amplitudes within a complete time cycle. (This can be different in other models.) During one cycle, two new upwellings are born on the left, generating peaks in the curve of Fig. 11(c). A third peak is caused by the merger of a travelling warm upwelling into the rightmost one at the box side. When the dip of the slope, G is larger, the picture becomes simpler: fewer rolls develop in the same box.

The second type of 2-D flow occurs at large values of G: then there are no moving rolls, the flow evolves to a steady state. The region of this type of 2-D circulation in the (G, R) plane is situated in the far right side (Fig. 9). This flow shows a 'unicell' structure: it has one downwelling (at the top of the slope) and one upwelling (at the other end of the slope), just as in a purely hydraulic situation. The pattern for $\varepsilon = 1$, $L_x = 7.2$, $R = 60$ and $G = 20$ can be seen in Fig. 12. These parameters, except for the large value of G, are the same as in Fig. 11. Although qualitatively the flow is the same as the flow without thermal buoyancy ($R = 0$), quantitatively it is different, because the heat expansion also contributes to the driving

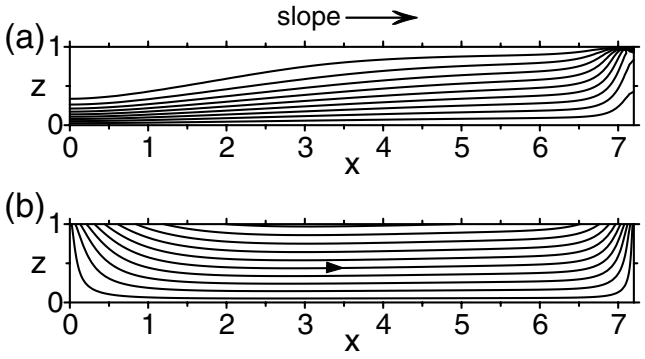

Figure 12. Steady-state unicell flow for $\varepsilon = 1$, $R = 60$, $G = 20$ in a box of length $L_x = 7.2$. Upper panel: isotherms, lower panel: streamlines.

force. As a result, the recharge zone is cooler and the discharge zone is warmer than it would be with $R = 0$. The Nusselt number Nu, which expresses the efficiency of the heat transfer, is also larger: at $G = 20$ and $R = 60$ it is $Nu = 1.842$; at $G = 20$ and $R = 0$ it would be $Nu = 1.692$. (At $G = 0$ and $R = 0$, the Nusselt number is 1.)

Characteristics of the heat transport when $G > 0$

If R increases at a fixed G, the surface heat flux (Nu) also increases. The increase is not monotonic, because the structure of the groundwater flow changes as the boundaries of the stability regions are crossed in the (G, R) plane (Fig. 9). The variation of Nu is shown for $G = 10$ in Fig. 13(a). The other parameters are $\varepsilon = 1$ and $L_x = L_y = 7.2$ as in the models of Figs 8, 10(a), 11 and 12. The first section of the curve in Fig. 13(a) corresponds to the 2-D unicell flow at very small values of R: the Nusselt number increases very slowly here. Then, in the region of the 2-D transverse rolls and later for the 3-D flows, Nu increases quickly. In a short interval at $R = 76$–89, longitudinal rolls yield the stable solution and Nu falls back slightly in this region.

The results are a little bit more complicated if Nu is plotted as a function of G, at fixed R. For the same circumstances as in Fig. 13(a), i.e. for $\varepsilon = 1$ and $L_x = L_y = 7.2$, Fig. 13(b) shows two curves fixing $R = 60$ and $R = 120$. In the range where thermal buoyancy contributes significantly to the flow (3-D cells, longitudinal rolls, 2-D transverse rolls), the general tendency is that Nu decreases with the increase of G. The decrease is not monotonic, because the flow structure changes several times as G increases. As we reach the unicell 2-D region, Nu begins to increase. The structure of the flow does not change any more. With increasing G, the velocity of the unicell flow increases, and it can transport more and more heat to the surface. On the contrary, at smaller G values, where more convective cells are present, the background hydraulic flow hinders the heat transport of the more efficient cellular convection, and this leads to the decrease of Nu with increasing G.

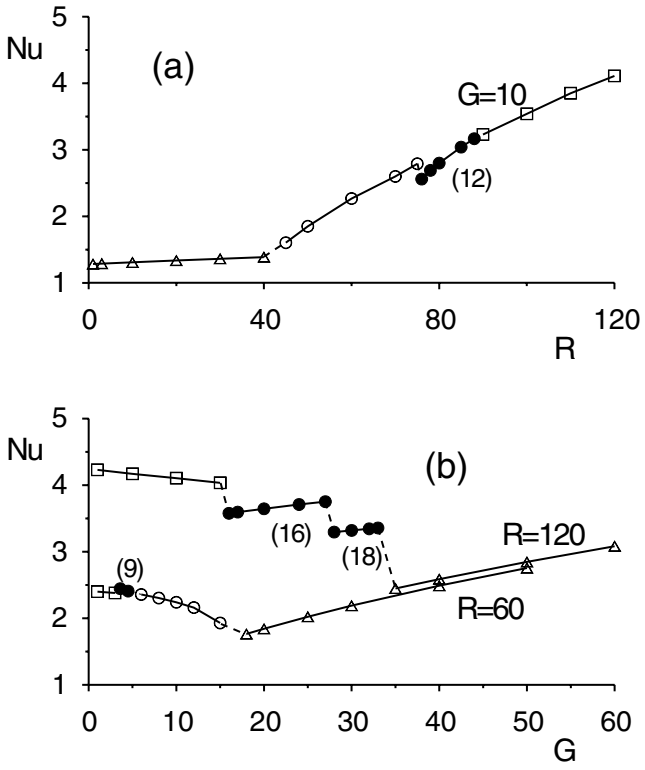

Figure 13. Variation of the Nusselt number (heat flux) in models with a square box $L_x = L_y = 7.2$ and isotropic medium ($\varepsilon = 1$), (a) for fixed G, (b) for fixed R. The curves show discontinuities because of abrupt changes in the flow pattern. Symbols: open squares, time-dependent polygonal cells; solid circles, steady-state longitudinal rolls; open circles, drifting transverse rolls; triangles, 2-D unicell flow. Nu is time averaged for time-dependent solutions. Numbers in parentheses indicate the number of longitudinal rolls that develop in the box of size $L_x = L_y = 7.2$.

DISCUSSION AND CONCLUSIONS

The basic form of thermal convection in an unconfined layer is the one where the surface hydraulic gradient is zero ($G = 0$). Above the critical Rayleigh number the first stable convective form consists of 2-D rolls. This is generally true in homogeneous horizontal layers, not only in the unconfined reservoir studied here but also in porous layers with impermeable boundaries (Steen 1983) and in Newtonian convection (Busse & Whitehead 1971). In the unconfined layer, when R increases, 3-D cells become stable very soon. We have established by numerical experiments the critical Rayleigh numbers for 3-D cells as the function of the cell size and anisotropy. In the numerical experiments, where we use rectangular boxes, we obtain square cells. It can be expected, however, that in an infinite layer hexagonal cells are stable under the same conditions as the squares. Since the hexagonal geometry does not fit the rectangular model boxes, we did not carry out experiments with hexagons. Experiments in porous layers (Bories & Combarnous 1973) or analogies with Newtonian convection (Busse & Frick 1985) indicate that the hexagonal cells are stable under more or less the same conditions as square cells. The topological characteristics of these two regular polygonal cells are basically the same. In a real experiment it is difficult to reproduce perfect regularity (Bories & Combarnous 1973). It is achieved usually by prescribing regular initial conditions. In ordinary circumstances, e.g. in case of irregular initial conditions ('noise'), the final polygons are irregular and they never reach the steady state. Some cells disappear and new ones are born continuously. At very high Rayleigh numbers, time dependence is obtained even in case of regular initial conditions: the initial regular cells disappear, showing that there is an upper limit for their stability on the scale of the Rayleigh number.

A common feature of either the regular or irregular polygonal cells in an unconfined layer at $G = 0$ is that a wide cold downwelling occupies the centre of the cells and a narrower warm upwelling belt is located all along the sides of a cell. There is therefore an inherent asymmetry: the downwellings and upwellings have different geometries. The reason for the asymmetry is that different boundary conditions prevail on the boundaries: the upper one is permeable and lower one is impermeable. In contrast, the structure of the convection cells in a layer confined by impermeable boundaries is symmetric, the downgoing and upgoing currents are mirror images of each other.

When there is a hydraulic slope on the surface ($G > 0$), the conditions for the appearance of cellular convection become stricter, because the hydraulic driving force competes with the buoyancy force in optimizing the heat transport or energy balance. As G increases, the critical Rayleigh number, above which there are cellular convective forms superimposed on the hydraulic background flow, also increases. Below the critical value (in the lowest domain in Fig. 9) 2-D 'unicell' flow occurs. It has a single downwelling below the upper end of the slope and a single upwelling below the lower

end of the slope. There is horizontal flow only in the direction of the slope. In this domain of the (G, R) space, even if $R > 0$, the buoyancy force is not strong enough to produce convective cells because the hydraulic flow sweeps them away. The unicell flow is the same qualitatively as the purely hydraulic flow at $G > 0$ and $R = 0$.

As R increases at a fixed value of $G(>0)$, the first cellular form of convection can appear in two different forms. For small anisotropy (approximately for $\varepsilon \leq 10$) and in a certain range of G, transverse rolls develop: this is a 2-D time-dependent flow where the rolls drift in the direction of the slope. In other cases, e.g. for large anisotropy, the first cellular form means longitudinal rolls. This is an important flow structure at all anisotropies. A further increase of R results in 3-D polygonal cells. These cells usually vary with time and travel along the slope, driven by the regional flow due to the hydraulic gradient.

The longitudinal rolls represent a transitional mode between the hydraulic flow and the 3-D polygonal convection. When G/R is large, the dominant mode is the hydraulic flow. When G/R is small and R is large enough, the dominant mode is 3-D convection. When G/R is in an intermediate range, the hydraulic gradient and the buoyancy force are equally important in governing the structure of the flow, and this results in longitudinal rolls. Buoyancy-driven convection interferes to the least extent possible with the hydraulic flow if they act in perpendicular directions. The hydraulic flow 'has no choice', it has to follow the direction of the slope, so thermal buoyancy is forced to select the transverse direction in order to optimize the energy transport. The outcome of this pattern selection problem is that convection is organized in rolls with their axes oriented parallel to the slope.

This type of convection has many analogies from other fields of fluid dynamics. When the atmosphere is thermally unstable and there is a regional wind, convection develops perpendicularly to the wind, producing spectacular cloud patterns with parallel stripes of clouds and cloudless zones which alternate periodically (Turner 1973; Tritton 1977). Richter & Parsons' (1975) experiments showed that a plate moving on the top of a horizontal layer of fluid produces longitudinal convective rolls in the fluid. Numerical studies supported these observations (Cserepes & Christensen 1990). Hart (1971) obtained longitudinal cells in a dipping fluid layer bounded by isothermal impermeable boundaries. In this case the 'regional wind' is produced by the tilted isothermal boundaries: the buoyancy force has a component in the direction of the dip even at infinitesimally low Rayleigh numbers. At supercritical Rayleigh numbers, local convection must act perpendicularly to the regional flow, and this leads again to longitudinal rolls. The same phenomenon has been observed in a dipping porous layer (Bories & Combarnous 1973; Caltagirone & Bories 1985; Ormond & Genthon 1993).

In the numerical experiments we used random initial perturbations. Depending on the G/R ratio a large selection occurs towards preferential directions in the convection: parallel to the slope, perpendicular to the slope and both directions in the case of transverse rolls, longitudinal rolls and 3-D polygonal cells respectively.

In this paper we investigated the structure of the water flow in an unconfined porous layer, which is bounded on the top by a hydraulic slope. We can conclude that the structure of the flow depends on the interaction between the driving forces: the hydraulic gradient and the buoyancy forces. The hydraulic gradient is determined by the dip of the slope, G, and the buoyancy force is characterized by the Rayleigh number R. We have established three different regions in the (G, R) plane, where fundamentally different flow structures exist, which depend on the G/R ratio. These basic forms are: 3-D polygonal cells at low G values, longitudinal cells for medium G/R, and 'unicell' 2-D flow for high G/R.

ACKNOWLEDGMENTS

To our great sorrow Professor László Cserepes died at the end of 2002. He was a well known scientist in mantle convection modelling, but he also made some 'excursions' to other fields of geophysics, e.g. modelling flow in porous media. Besides, he was an excellent teacher. We, his colleagues and students, will miss him. We thank C. Thorenz and an anonymous reviewer for their helpful comments. This work has been supported by the Hungarian Science Foundation grant No. T037980. LL acknowledges the financial support given by the János Bolyai Fellowship.

REFERENCES

Alföldi, L., Erdélyi, M., Gálfi, J., Korim, K. & Liebe, P., 1976. Hydrogeological and geophysical investigations of a geothermal anomaly in Hungary. II. Geothermal flow system in the Tiszakécske region, *Bull. Hydrol. Sci.,* **21,** 1–13.

Bear, J. & Verruijt, A., 1987. *Modeling Groundwater Flow and Pollution*, p. 414, Reidel, Dordrecht.

Beck, J.L., 1972. Convection in a box of porous material saturated with fluid, *Phys. Fluids,* **15,** 1377–1383.

Bernard, D., 1988. Convection naturelle dans une couche géologique poreuse inclinée, in *Computer Methods and Water Resources,*Computational Transport Phenomena**Vol. 5,** pp. 59–70, eds. Ouazar, D. & Brebbia, C.A., Springer, Berlin.

Bolton, E.W. & Busse, F.H., 1985. Stability of convection rolls in a layer with stress-free boundaries, *J. Fluid Mech.,* **150,** 487–498.

Bories, S.A. & Combarnous, M.A., 1973. Natural convection in a sloping porous layer, *J. Fluid Mech.,* **57,** 63–79.

Bus, Z. & Cserepes, L., 1994. Three-dimensional forms of thermal convection in porous layers, *Acta Geod. Geophys. Hung.,* **29,** 209–220.

Busse, F.H. & Frick, H., 1985. Square-pattern convection in fluids with strongly temperature-dependent viscosity, *J. Fluid Mech.,* **150,** 451–465.

Busse, F.H. & Whitehead, J.A., 1971. Instabilities of convection rolls in a high Prandtl number fluid, *J. Fluid Mech.,* **47,** 305–320.

Caltagirone, J.P. & Bories, S., 1985. Solutions and stability criteria of natural convective flow in an inclined porous layer, *J. Fluid Mech.,* **155,** 267–287.

Celati, R., Grassi, S. & Calore, C., 1990. Overflow thermal springs of Tuscany (Italy), *J. Hydrol.,* **118,** 191–207.

Celati, R., Grassi, S., D'Amore, F. & Marcolini, L., 1991. The low temperature hydrothermal system of Campiglia, Tuscany (Italy): a geochemical approach, *Geothermics,* **20,** 67–81.

Clauser, C. & Villinger, H., 1990. Analysis of conductive and convective heat transfer in a sedimentary basin, demonstrated for the Rheingraben, *Geophys. J. Int.,* **100,** 393–414.

Cserepes, L. & Christensen, U., 1990. Three-dimensional convection under drifting plates, *Geophys. Res. Lett.,* **17,** 1497–1500.

Cserepes, L., Rabinowicz, M. & Rosemberg-Borot, C., 1988. Three-dimensional infinite Prandtl number convection in one and two layers with implications for the Earth's gravity field, *J. geophys. Res.,* **93,** 12 009–12 025.

Davis, E.E., Chapman, D.S. & Forster, C.B., 1996. Observations concerning the vigor of hydrothermal circulation in young oceanic crust, *J. geophys. Res.,* **101,** 2927–2942.

Deming, D., 1993. Regional permeability estimates from investigations of coupled heat and groundwater flow, North Slope of Alaska, *J. geophys. Res.,* **98,** 16 271–16 286.

Domenico, P.A. & Palciauskas, V.V., 1973. Theoretical analysis of forced convective heat transfer in regional ground-water flow, *Geol. soc. Am. Bull.,* **84,** 3803–3814.

Erdélyi, M., 1985. Geothermics and the deep flow-system of the Hungarian basin, *J. Geodyn.,* **4,** 321–330.

Fisher, A.T., Becker, K., Narasimhan, T.N., Langseth, M.G. & Motl, M.J., 1990. Passive off-axis convection through the southern flank of the Costa Rica rift, *J. geophys. Res.,* **95,** 9343–9370.

Graham, M.D. & Steen, P.H., 1991. Structure and mechanism of oscillatory convection in a cube of fluid-saturated porous material heated from below, *J. Fluid Mech.,* **232,** 591–609.

Harris, R.N., Garven, G., Georgen, J., McNutt, M.K., Christiansen, L. & Von Herzen, R.P., 2000. Submarine hydrogeology of the Hawaiian archipelagic apron 2. Numerical simulations of coupled heat transport and fluid flow, *J. geophys. Res.,* **105,** 21 371–21 385.

Hart, J.E., 1971. Stability of the flow in a differentially heated inclined box, *J. Fluid Mech.,* **47,** 547–576.

Holst, P.H. & Aziz, K., 1972. Transient three-dimensional natural convection in confined porous media, *Int. J. Heat Mass Transfer,* **15,** 73–90.

Kimura, S., Schubert, G. & Straus, J.M., 1989. Time-dependent convection in a fluid-saturated porous cube heated from below, *J. Fluid Mech.,* **207,** 153–189.

Lenkey, L., 1993. Study of the thermal anomaly at Tiszakécske by numerical modelling of the thermal convection, (In Hungarian with English abstract.), *Magyar Geofiz.,* **34,** 30–45.

Marsily, G. de, 1986. *Quantitative Hydrogeology*, p. 440, Academic Press, New York.

Ormond, A. & Genthon, P., 1993. 3-D thermoconvection in an anisotropic inclined sedimentary layer, *Geophys. J. Int.,* **112,** 257–263.

Rabinowicz, M., Boulègue, J. & Genthon, P., 1998. Two- and three-dimensional modeling of hydrothermal convection in the sedimented Middle Valley segment, Juan de Fuca Ridge, *J. geophys. Res.,* **103,** 24 045–24 065.

Remson, I., Hornberger, G.M. & Molz, F.J., 1971. *Numerical Methods in Subsurface Hydrology*, Wiley-Interscience, New York.

Ribando, R.J., Torrance, K.E. & Turcotte, D.L., 1976. Numerical models for hydrothermal circulation in the oceanic crust, *J. geophys. Res.,* **81,** 3007–3012.

Richter, F.M. & Parsons, B., 1975. On the interaction of two scales of convection in the mantle, *J. geophys. Res.,* **80,** 2529–2541.

Rosenberg, N.D. & Spera, F.J., 1990. Role of anisotropic and/or layered permeability in hydrothermal convection, *Geophys. Res. Lett.,* **17,** 235–238.

Schubert, G. & Straus, J.M., 1979. Three-dimensional and multicellular steady and unsteady convection in fluid-saturated porous media at high Rayleigh numbers, *J. Fluid Mech.,* **94,** 25–38.

Smith, L. & Chapman, D.S., 1983. On the thermal effects of groundwater flow: 1. Regional scale systems, *J. geophys. Res.,* **88,** 593–608.

Stamps, D.W., Arpaci, V.S. & Clark, J.A., 1990. Unsteady three-dimensional natural convection in a fluid-saturated porous medium, *J. Fluid Mech.,* **213,** 377–396.

Steen, P.H., 1983. Pattern selection for finite-amplitude convection states in boxes of porous media, *J. Fluid Mech.,* **136,** 219–241.

Straus, J.M. & Schubert, G., 1979. Three-dimensional convection in a cubic box of fluid-saturated porous material, *J. Fluid Mech.,* **91,** 155–165.

Tritton, D.J., 1977. *Physical Fluid Dynamics*, p. 362, Van Nostrand Reinhold, New York.

Turner, J.S., 1973. *Buoyancy Effects in Fluids*, p. 368, Cambridge University Press, Cambridge.

Wang, K., He, J. & Davis, E.E., 1997. Influence of basement topography on hydrothermal circulation in sediment-buried igneous oceanic crust, *Earth planet. Sci. Lett.,* **146,** 151–164.

Willett, S.D. & Chapman, D.S., 1987. Temperatures, fluid flow and the thermal history of the Uinta Basin, in *Migration of Hydrocarbons in Sedimentary Basins*, pp. 533–551, ed. Doligez, B., Technip, Paris.

Williams, D.L., Von Herzen, R.P., Sclater, J.G. & Anderson, R.N., 1974. The Galapagos spreading centre: lithospheric cooling and hydrothermal circulation, *Geophys. J. R. astr. Soc.,* **38,** 587–608.

Williams, C.F., Narasimhan, T.N., Anderson, R.N., Zoback, M.D. & Becker, K., 1986. Convection in the oceanic crust: simulation of observations from Deep Sea Drilling Project Hole 504B, Costa Rica Rift, *J. geophys. Res.,* **91,** 4877–4889.

Woodbury, A.D. & Smith, L., 1985. On the thermal effects of three-dimensional groundwater flow, *J. geophys. Res.,* **90,** 759–767.

APPENDIX

The general governing equations of thermal convection in a permeable medium are the equation of continuity, Darcy's law and the heat transport equation (Marsily 1986; Bear & Verruijt 1987):

$$\frac{\partial(n\rho)}{\partial t} + \nabla(\rho\mathbf{u}) = 0 \tag{A1}$$

$$-\rho g\mathbf{e} - \nabla p - \eta\boldsymbol{k}^{-1}\mathbf{u} = 0 \tag{A2}$$

$$\chi\frac{\partial T}{\partial t} + \mathbf{u}\nabla T = \kappa\nabla^2 T. \tag{A3}$$

For notation see main text.

In the case of an unconfined (i.e. near-surface) reservoir the use of the classical Boussinesq approximation can be admitted. Then the density of water ρ is assumed to depend only on the temperature and only in eq. (A2):

$$\rho = \rho_0(1 - \alpha T) \tag{A4}$$

where ρ_0 is the density of water at $T = 0$ and α is the thermal expansion coefficient of water. Otherwise ρ is constant together with the other parameters of the medium. Thus eqs (A1) and (A2) become:

$$\nabla\mathbf{u} = 0 \tag{A5}$$

$$-\rho_0(1 - \alpha T)g\mathbf{e} - \nabla p - \eta\boldsymbol{k}^{-1}\mathbf{u} = 0. \tag{A6}$$

Eq. (A5) says that $\mathbf{u}$ is a solenoidal vector field, therefore it can be decomposed as:

$$\mathbf{u} = \nabla \times \nabla \times V\mathbf{e} + \nabla \times W\mathbf{e} \tag{A7}$$

where V and W are the poloidal and toroidal potentials, respectively. From eq. (A6) $\mathbf{u}$ can be written as:

$$\mathbf{u} = \frac{\mathbf{k}}{\eta}[\alpha\rho_0 gT\mathbf{e} - \nabla(p + \rho_0 gz)] = \boldsymbol{K}\mathbf{e}\alpha T - \boldsymbol{K}\nabla h \tag{A8}$$

where $\boldsymbol{K}$ is the hydraulic conductivity defined as:

$$\boldsymbol{K} = \frac{\rho_0 g}{\eta}\boldsymbol{k} \tag{A9}$$

and h is the piezometric head:

$$h = \frac{p}{\rho_0 g} + z. \tag{A10}$$

We assume a homogeneous but anisotropic medium, restricting anisotropy to the simple symmetric case where the hydraulic conductivity tensor appears as:

$$\boldsymbol{K} = K_0\begin{bmatrix} 1 & 0 & 0 \\ 0 & 1 & 0 \\ 0 & 0 & 1/\varepsilon \end{bmatrix}. \tag{A11}$$

Here K_0 and $\varepsilon > 1$ are constant values. This form means that the only deviation from isotropy is that the hydraulic conductivity is smaller vertically than horizontally. ε is the anisotropy coefficient. It is defined as the ratio of horizontal to vertical conductivities. Eq. (A11) is a good approximation in the case of a horizontally layered medium where layering is so fine that the medium looks

homogeneous macroscopically. Since the permeability differs from the hydraulic conductivity in a constant (eq. A9), the form of the permeability tensor is the same as eq. (A11), except that k_0 is in the equation.

Calculating the vorticity of $\mathbf{u}$ from eq. (A8) as $\omega = \text{rot}\ \mathbf{u}$, its vertical component becomes zero due to the form of the hydraulic conductivity tensor (eq. A11):

$$\omega_z = \mathbf{e}\nabla \times \mathbf{u} = 0. \tag{A12}$$

Note that if the medium were not isotropic horizontally, then ω_z would not be zero.

Taking the curl of $\mathbf{u}$, it follows from eqs (A7) and (A12) that W is constant, so there is no toroidal component of $\mathbf{u}$:

$$\mathbf{u} = \nabla \times \nabla \times V\mathbf{e}. \tag{A13}$$

$\mathbf{u} = (u, v, w)$ can be derived from V as, (eq. 7 in main text):

$$u = \frac{\partial^2 V}{\partial x \partial z}, \quad v = \frac{\partial^2 V}{\partial y \partial z}, \quad w = -\left(\frac{\partial^2 V}{\partial x^2} + \frac{\partial^2 V}{\partial y^2}\right). \tag{A14}$$

Finally, by taking the curl of eq. (A6) and using eqs (A11) and (A14), we arrive at a differential equation for V:

$$\varepsilon\left(\frac{\partial^2 V}{\partial x^2} + \frac{\partial^2 V}{\partial y^2}\right) + \frac{\partial^2 V}{\partial z^2} = -K_0 \alpha T. \tag{A15}$$

The boundary conditions have been defined in the description of the model. Let us now redefine them for V. The impermeable bottom means that $w = 0$. From eq. (A14) it follows that:

$$V = 0 \quad \text{at} \quad z = 0. \tag{A16}$$

The upper boundary of the reservoir is the surface of the water table:

$$z = D + H(x, y)$$
$$H(x, y) = -\gamma(x - D_x/2) \quad (\gamma \geq 0) \tag{A17}$$

where $H(x, y)$ is the elevation of the water table with respect to its mean position $z = D$. It dips in the x direction and its slope is a constant, γ. Assuming that $H \ll D$, the piezometric head at the top of the computational domain ($z = D$) is:

$$h \approx D + H \quad \text{at} \quad z = D. \tag{A18}$$

The upper boundary conditions will be defined for the $z = D$ plane:

$$T = 0 \quad \text{at} \quad z = D. \tag{A19}$$

From eq. (A18), using eqs (A8) and (A11):

$$u = -K_0 \frac{\partial H}{\partial x} \quad \text{at} \quad z = D. \tag{A20}$$

Applying eq. (A14) for eq. (A20), we arrive at the boundary condition for V:

$$\frac{\partial V}{\partial z} = -K_0 H = K_0 \gamma (x - D_x/2) \quad \text{at} \quad z = D. \tag{A21}$$

Eqs (A3), (A14) and (A15) and the boundary conditions are used in dimensionless form during the computations. The scaling factors are D for the distance, D^2/κ for time, κ/K_0 for the piezometric head and ΔT for the temperature. The dimensionless equations (eqs 4–7) and boundary conditions (eqs 8, 10–12) are shown in the main text.